Catalysis Science & Technology

ROYAL SOCIETY OF CHEMISTRY

PAPER

View Article Online
View Journal | View Issue

Check for updates

Cite this: *Catal. Sci. Technol.*, 2024, 14, 6678

Enhancing coking resistance of nickel-based catalysts for dry reforming of methane *via* nitric oxide abatement: a support study†

Beatrice Senoner, *[a] Andrea Osti [a] and Antonella Glisenti [ab]

Received 29th July 2024,
Accepted 24th September 2024

DOI: 10.1039/d4cy00936c

rsc.li/catalysis

Coking poses a significant challenge to the longevity and efficacy of catalysts in dry reforming of methane (DRM), particularly for nickel-based catalysts, which are widely used for their affordability and high catalytic activity. This study explores a recent approach integrating DRM with NO reduction to address coking-related deactivation, aiming to gasify carbon deposits and reduce NO simultaneously. Therefore, herein, NO conversion is achieved using the carbon undesired by-product of the DRM reaction, avoiding the use of valuable resources for NO conversion (such as NH_3), *via* an approach "from waste to value" that enhances the sustainability of the process. Four nickel-impregnated oxide supports (γ-Al_2O_3, $MgAl_2O_4$ coated γ-Al_2O_3, $CaZrO_3$, and $LaFeO_3$) were compared to understand the key properties of catalyst design. The best performances were obtained for supports with a high surface area and high interaction with metal particles (95% reactant conversion for Ni/γ-Al_2O_3) as they allowed stable activity and protection from NO oxidation. Supports with a lower surface area suffered from coke blockage of active sites, whereas no protection from oxidation led to complete deactivation of the active phase. The $LaFeO_3$ support stood out for its ability to protect Ni from NO oxidation by reducing NO. Overall, this study showed the importance of balancing NO oxidative power and coking issues, emphasizing the relevance of catalyst design in both protecting Ni from NO oxidation and avoiding coke blockage of the active sites *via* high surface area supports.

1. Introduction

Dry reforming of methane (DRM) is a dream reaction that allows the conversion of two pollutants/greenhouse gases into a highly energetic gas mixture: syngas. One of the most commonly used active metals is nickel, which provides comparable activity to noble metals, without the heavy cost and availability problems of the latter.[1,2] However, nickel catalysts are sensitive to deactivation by coking and sintering; thus, to develop catalysts with industrial applicability, extending their lifetime is one of the key requirements.[3–5] In this project, catalysts were studied for a process in which dry reforming of methane and nitric oxide reduction reactions are involved. The reactions involved in the process are presented below:

$$CH_4\,(g) + CO_2\,(g) \rightarrow 2CO\,(g) + 2H_2\,(g) \quad (1)$$

$$CO_2\,(g) + H_2\,(g) \rightarrow CO\,(g) + H_2O\,(g) \quad (2)$$

$$CH_4\,(g) \rightarrow 2C\,(s) + 2H_2\,(g) \quad (3)$$

$$C\,(s) + CO_2\,(g) \rightarrow 2CO\,(g) \quad (4)$$

$$C\,(s) + xNO\,(g) \rightarrow CO_x\,(g) + \frac{x}{2}N_2\,(g)\ (x = 1 \text{ or } 2). \quad (5)$$

Coupling these two reactions (1) and (5) eliminates carbon that deposits onto catalysts during DRM (reaction (3)) by exploiting the oxidizing power of one of the largest pollutants in the atmosphere, whose emissions have reached a scale of millions of tons per year: nitric oxide.[6] This process was tested for the first time by Hu *et al.* with Ni/α-Al_2O_3 and stands out because it can simultaneously abate three main pollutants/greenhouse gases: CO_2, CH_4 and NO.[7] Syngas production (reaction (1)) can therefore be combined with exhaust treatment (reaction (5)), providing a highly efficient strategy useful for industrial applications as it allows the consumption of energy needed by the two processes to be diminished by coupling them into one. Moreover, this process provides an interesting solution for NO abatement as the deposited carbon is employed here to convert NO into N_2

[a] *Dipartimento di Scienze Chimiche, Università degli Studi di Padova, Via F. Marzolo, 1, 35131, Padova, Italy. E-mail: beatrice.senoner@phd.unipd.it*
[b] *ICMATE – CNR c/o Dipartimento, Italy*

† Electronic supplementary information (ESI) available. See DOI: https://doi.org/10.1039/d4cy00936c

(reaction (5)), thereby avoiding the employment of higher economic value substances. Although currently employed reductants are substances of high economic value, such as NH_3, H_2, CO or hydrocarbons, NO is reduced by coke, allowing this undesired by-product of DRM to become a useful reactant.[8–11] The process showed good performance, especially for the "CMN" process (chemical looping methane–nitric oxide dry reforming), where DRM and NO reduction processes were alternated every 10 minutes.[7] However, the alternation of fluxes is a factor that increases the complexity of the system; therefore, it is crucial to enhance the performances of the so-called single-step reaction process (SSR), *i.e.* where CH_4, CO_2, and NO are all fluxed simultaneously, to allow easy industrial applicability of the process. To enhance the performance of the SSR process and its applicability, a support study was carried out to allow higher conversions and to understand which properties of the supports are essential in catalyst design. Enhancing the catalytic activity is key to having a highly efficient industrial process; therefore, supports with Lewis basicity properties were studied to enhance CO_2 conversions and coke gasification.[12,13] Furthermore, the type of support determines the interaction with nickel nanoparticles, influencing their size and stability.[2,14] To appreciate the impact of these properties on the process, γ-Al_2O_3, $MgAl_2O_4$ coated with γ-Al_2O_3, $CaZrO_3$ and $LaFeO_3$ were compared. The supports are all polycationic oxides chosen for their low-cost, availability, and possibility to be synthesized *via* eco-friendly wet-chemistry synthesis.[15–18] Alumina is designated as the first support and is a standard support for DRM owing to its high surface area values, stability in the DRM atmosphere and low cost. In particular, gamma alumina was chosen owing to its strong interaction with Ni particles, which helps in controlling nickel particle size and stability. However, this support is mildly acidic, making it more susceptible to coking and less favorable for CO_2 conversion.[19–21] Therefore, a second support with Lewis basicity was chosen to enhance carbon gasification: $MgAl_2O_4$. This support has high interaction with metal particles, which are interesting properties for enhancing DRM activity and preventing excessive coking.[22,23] This is due to CO_2 being a mildly acidic molecule; therefore, it can better interact with a basic support, and starting from the coordination of this molecule on the support, its conversion increases not only to obtain syngas (reaction (1)) but also to react with coke (reaction (4)). In particular, a $MgAl_2O_4$ coating on Al_2O_3 was chosen, which allowed for both having an alumina high surface area and the basicity of the coating spinel. Alumina-based materials have been compared to another class of oxides, perovskites, which are materials known for their flexible nature, allowing for tuning of the desired properties based on the choice of the metal cations.[24,25] Perovskite $CaZrO_3$ was chosen owing to its high thermal stability and the presence of alkali metal cations that enhance Lewis basicity, leading to better CO_2 chemisorption ability.[25–27] Finally, a final support was selected with the aim of studying the process with a support employed in NO_x removal: $LaFeO_3$. In particular, this perovskite support is active towards NO removal, therefore giving the opportunity to study a modified NO interaction with the catalyst.[28]

In this work, we prepared and investigated the activity in the DRM–NO reduction process of four supported catalysts, with the support being the oxides described above, and the active metal being Ni. The 13 wt% Ni impregnation has been chosen as a value inside the standard percentage range of 10–15% for industrial application of DRM, as reported in the literature.[29–31] The physical and chemical properties of the catalysts were analyzed by N_2-physisorption, H_2-temperature programmed reduction (H_2-TPR), H_2-pulsed chemisorption, X-ray diffraction (XRD), XPS (X-ray photoelectron spectroscopy), and SEM-EDX (scanning electron microscopy-energy dispersive X-ray) to gain insight into the catalyst's properties. With the analysis above, the relationship between catalytic activity and structure was established. Furthermore, O_2-temperature programmed oxidation (O_2-TPO), XRD and XPS techniques were applied to post-reaction catalysts to examine the change in the catalysts induced by the process.

2. Experimental

2.1. Synthesis of catalysts

Catalysts were prepared *via* wet-chemical environmentally friendly synthesis using water as solvent. In the first step, the support was obtained (around 3 g); then, nickel oxide nanoparticles were deposited in the second step. To obtain the active form of the catalyst, a 5% H_2 treatment was needed to reduce nickel oxide and obtain metallic nickel.

2.1.1. Supports. Four supports are considered. Commercial γ-Al_2O_3 was used as the first support (Merck, 99.95%), while the other three were obtained *via* wet chemistry routes. The second support is $MgAl_2O_4$ spinel-coated γ-Al_2O_3 obtained *via* a coprecipitation synthesis using $Mg(OH)_2$ (Sigma-Aldrich, 95%) and γ-Al_2O_3 (Merck, ≥99.95%) precursors of the metals in stoichiometric amounts. $Mg(OH)_2$ was dissolved in around 50 mL of H_2O with a stoichiometric amount of HNO_3 (65%, Sigma-Aldrich) to obtain the corresponding nitrate salt. Then, γ-Al_2O_3 was suspended in approximately 150 mL of H_2O and added to the previous solution to obtain a ratio $MgAl_2O_4$/Al_2O_3 of 25 wt%. The dispersion was heated at 80 °C overnight under stirring until complete evaporation; then, the product was ground, and the obtained powder was calcined at 900 °C for 6 h to obtain the spinel-alumina phase. The two perovskite supports were synthesized *via* a citrate self-combustion route.[32] Stoichiometric quantities of metal cations were dissolved in approximately 50 mL of water for each cation, and HNO_3 was used in stoichiometric amounts to dissolve the cations if needed. Citric acid monohydrate (Sigma-Aldrich, <99.0%) was then dissolved in around 50 ml of H_2O and added to the solution of the cations to coordinate the cations as a complexing agent. The solution was then heated at around 100 °C under stirring conditions and basified with NH_4OH (Sigma-Aldrich, 28–30%) drop by drop until pH 7–8

for better homogeneous dispersion of the metal cations owing to the complete deprotonation of citric acid. The solvent was evaporated until a solution volume of around 100 mL was reached. Then, the solution was transferred to a metal beaker and heated for water evaporation to allow gel formation (network of metal cations/metal nitrates linked with citrate ligands). The gel was dried overnight at around 100 °C and then heated at 300 °C to obtain self-combustion (due to the exothermic decomposition of NH_4NO_3 formed from the reaction between nitric acid and ammonia), which then causes the decomposition of all the organic content, with the development of gaseous products (CO_2, H_2O and NO_x). The formed porous solid was ground to obtain a powder, which was finally calcined to obtain the perovskite phase. $CaZrO_3$ was obtained starting from precursors $ZrO(NO_3)_2$ and $Ca(CO_3)_2$ (Sigma-Aldrich, ≥99%); minimum quantities of HNO_3 were used to dissolve $Ca(CO_3)_2$. Citric acid was used in a citric acid/total number of cations molar ratio of 1.9, a ratio previously optimized by the research group.[33] The product was calcined in a muffle for 6 h at 1400 °C (heating rate: 5 °C min^{-1}) to obtain minimum impurities. $LaFeO_3$ was synthesized using as precursors La_2O_3 (Sigma-Aldrich, ≥99.9%) and $Fe(NO_3)_3{\cdot}9H_2O$ (Sigma-Aldrich, 98%), together with HNO_3 in minimum quantity to dissolve La_2O_3; citric acid was used in a molar ratio citric acid/total number of cations ratio of 1.1, as optimized by the research group for ferrites.[32] The product was calcined for 6 h at 800 °C (heating rate: 5 °C min^{-1}).

Supports were obtained with a yield of around 80–90%.

2.1.2. Nickel oxide nanoparticle deposition. Nickel oxide deposition was obtained by simple wet impregnation. A stoichiometric amount of precursor $Ni(NO_3)_2{\cdot}6H_2O$ was dissolved in around 20 mL of H_2O and then added to the suspension of the support in water (around 50 mL) to obtain catalysts with a loading of metallic nickel of 13 wt% after H_2-reductive treatment. All samples were dried at 80 °C overnight under stirring conditions and then kept for 2 hours at 100 °C to allow for the evaporation of water and nitrate, and the solid obtained was ground to powder. Finally, the samples were calcined at 650 °C for 6 hours (heating rate: 5 °C min^{-1}).

2.2. Characterization of catalysts

All catalysts were characterized using the following techniques. The chemical composition and crystalline phases of the samples were studied *via* X-ray diffraction (XRD) using a Bruker D8 Advance diffractometer with Bragg–Brentano geometry using Cu Kα radiation (40 kV, 40 mA, λ = 0.154 nm). Phase structures were assigned based on search-match software utilizing the COD-Inorg REV189751 database. X-ray photoelectron spectroscopy (XPS) analysis was performed to study the composition and phases of the surface of the samples *via* a Thermo Scientific ESCALAB QXi spectrometer, employing a monochromatized Al Kα source ($h\nu$ = 1486.68 eV) and a charge compensation gun. Survey spectra were acquired at pass energy 100 eV, resolution 0.5 eV per step, and dwell time 25 ms per step. Elemental quantification was carried out by the integration of photopeaks after Shirley-type background subtraction,[34] and the atomic percentage was evaluated using Thermo Scientific sensitivity factors.[35] For the correct interpretation of XPS spectra, the NIST XPS database was employed (version 4.1).[36] Energy-dispersive X-ray analysis (EDX) was obtained to gain information about the composition of the samples with a Zeiss SUPRA 40 V P microscope at 20 kV electron acceleration voltage, probing a large area of the sample (rectangle of hundreds of μm each side). N_2 physisorption analysis was conducted using a Micromeritics ASAP2020 analyser to gain information about the specific surface area (SSA) and porosity of the samples *via* BET analysis. Around 50 mg of the sample was degassed at 300 °C for 6 h under reduced pressure (around 0.013 mbar) before adsorption occurred. The analysis was conducted at −196 °C, collecting 80 points between p/p^0 = 0.002 and p/p^0 = 1. H_2-temperature programmed reduction (H_2-TPR, AutoChem II 2920) experiments were performed to determine the sample reducibility. Experiments were carried out in a U-shaped quartz reactor using 50 mg of sample and heating from RT to 900 °C or 600 °C at 10 °C min^{-1} under a constant flow of H_2 5% in Ar (50 ml min^{-1}). The same instrument was used to determine Ni dispersion *via* H_2-pulsed chemisorption. After reduction, the catalysts were cooled to 40 °C in the same environment, and H_2 was repeatedly pulsed 20 times at the same temperature. Finally, SEM-EDX maps were obtained with JEOL JEM-F200 TEM (200 kV).

2.3. Catalytic tests

Dry reforming of methane coupled with nitric oxide reduction was performed on the four samples in a quartz tube fix bed reactor (ID 6 mm) loaded with about 50 mg of catalyst sandwiched between two quartz wools, with a thermocouple mounted upstream of the bed. Two reaction mixtures were studied, composed of 5 CH_4, 5 CO_2, 1% NO and 25% CH_4, 25% CO_2, and 1% NO, using Ar as a balance for a total flow rate of 100 mL min^{-1} and a WHSV of about 120 L g^{-1} h^{-1}. Before the catalytic experiments, a reductive treatment was performed to obtain the active form of the catalysts using a 5% H_2 flow in Ar and increasing the temperature to 900 ° C for Al_2O_3-based samples and 600 °C for perovskite samples, as suggested by TPR measurements, with a ramp of 10 °C min^{-1}. Then, catalytic measurements were conducted at 750 °C. The reaction mixture was analyzed using an on-line Agilent Technologies 7890A gas-chromatograph, equipped with a TCD detector. A condenser to trap the generated water was employed between the reactor and GC.

2.4. Characterization of post-reaction catalysts

Catalysts were evaluated after the process with XRD and XPS analyses to appreciate the changes after the process. Raman

spectroscopy was used to study the coke deposition on a Thermo Scientific DXR Raman Microscope, with the excitation line λ = 532 nm. O_2-TPO (temperature-programmed oxidation) experiments were conducted to examine the quantity and type of coke deposited onto the catalyst during the catalytic tests. Around 20 mg of post-reaction catalysts were loaded between two quartz wools into a quartz tube reactor coupled with a thermocouple for the catalytic tests. Then, 25% air in Ar (5% O_2), for a total flow rate of 100 ml min^{-1} and a WHSV of about 240 L g^{-1} h^{-1}, was used to carry out the TPO measurements, while the temperature increased from room temperature to 900 °C (ramp of 2 °C min^{-1}). The reaction mixture was analyzed with an online Agilent Technologies 7890A gas chromatograph (GC), equipped with a TCD detector; a condenser was used to trap the generated water between the reactor and GC.

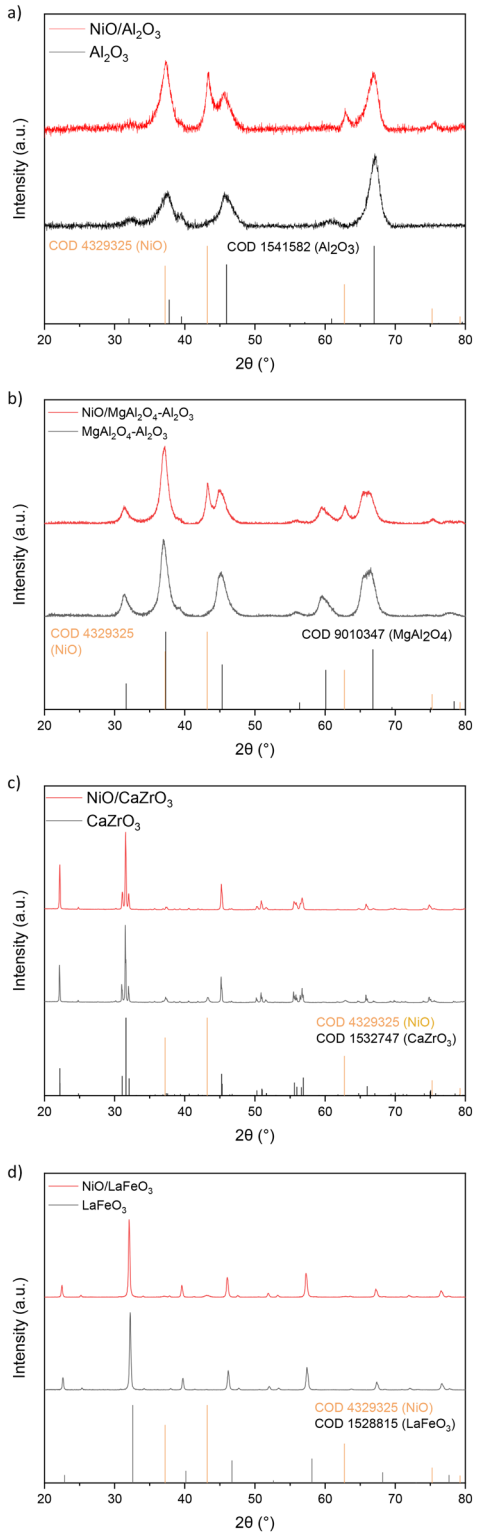

Fig. 1 XRD pattern of Al_2O_3 (a), $MgAl_2O_4$–Al_2O_3 (b), $CaZrO_3$ (c) and $LaFeO_3$ (d) synthetized supports after calcination and of the respective 13 wt% Ni impregnated catalysts.

3. Results and discussion

3.1. Catalyst characterization: XRD, N_2 physisorption, H_2-TPR and XPS techniques

3.1.1. X-ray diffraction (XRD). The XRD patterns of the four samples were studied to verify the correct phase formation. For each catalyst, both the support and the post impregnation samples were characterized, as shown in Fig. 1.

The four supports showed the correct synthesis of the supports, with only $CaZrO_3$ having traces of ZrO_2 impurities, due to unreacted ZrO_2 (Fig. 1(c)).[37] After impregnation, the catalysts showed the correct deposition of NiO. Moreover, in the alumina-based samples (Fig. 1(a) and (b)), the formation of $NiAl_2O_4$ spinel is possible due to nickel entering the alumina structure, as reported in the literature. However, its reflections could not be clearly detected as they are partially hindered by the alumina. For the $NiO/MgAl_2O_4$–Al_2O_3 sample (Fig. 1(b)), an additional contribution to the broad reflection at 2θ = 66° could be observed on the left side of the reflection after NiO impregnation, which could be because the $NiAl_2O_4$ phase overlapped with the Al_2O_3 and $MgAl_2O_4$ phases. Therefore, XPS analysis was performed to gain more information (subsubsection 3.1.4.).

3.1.2. N_2 physisorption. N_2 physisorption experiments were conducted to investigate the porosity and specific surface area of the catalysts. Linear plots of physisorption isotherms (see ESI†) were interpreted with the 1985 IUPAC classification.[38] Al_2O_3-based samples had isotherms between the type II and IVa shapes (Fig. S2(a) and (b)†) characterized by mesoporous materials and a macroporous or nonporous porosity, causing the amount of adsorbate to change to infinity at $p = p^0$. The hysteresis loop is type H1, *i.e.*

Table 1 BET surface areas of post-impregnation catalyst as determined *via* N_2-physisorption measurements

Sample	BET surface area (m^2 g^{-1})
NiO/Al_2O_3	105
$NiO/MgAl_2O_4$	62
$NiO/CaZrO_3$	3
$NiO/LaFeO_3$	6

associated with materials with uniform mesopores within a narrow range. However, perovskite samples (Fig. S2(c) and (d)†) showed a type III isotherm, which accounts for macroporous/nonporous porosity, and a hysteresis loop H1 type due to the presence of mesoporosity in the materials. Owing to the Brunauer–Emmett Teller method (BET), an estimation of the values of the surface area of the different samples can be made, as presented in Table 1.

Samples show different values of surface area based on the properties of the material and synthesis conditions (Table 1). As NiO deposition was done using the same synthesis conditions (13 wt%, 650 °C, 6 h), the catalyst differences between the supports caused a difference in the values of the surface area. Commercial Al_2O_3 support showed a higher surface area (104.7 m^2 g^{-1}) that diminished to approximately half its value when coated with $MgAl_2O_4$ (61.5 m^2 g^{-1}), which required an additional calcination treatment at 900 °C, with consequent sintering. Perovskite samples showed lower values of surface area, as expected for the intrinsic characteristics of these oxides.[25] Moreover, $CaZrO_3$ perovskite needed a high calcination temperature (1400 °C) to obtain low amounts of ZrO_2 impurities, so its surface area is the lowest (3.0 m^2 g^{-1}) due to sintering of the support. $LaFeO_3$ perovskite, however, was obtained as a pure crystalline phase using a calcination temperature of 900 °C, which allowed us to obtain higher surface areas (6.4 m^2 g^{-1}, double with respect to $CaZrO_3$). Finally, the desorption isotherms were allowed to conduct a BJH analysis to determine the pore size distribution (Fig. S1 in ESI†). BJH (Barrett, Joyner, and Halenda) analysis showed pores mainly distributed for NiO/Al_2O_3 and $NiO/MgAl_2O_4$–Al_2O_3 in the range of 3–9 nm, which accounts for the mesoporosity of alumina-based samples. Perovskite samples, however, have larger and fewer pores than alumina-based samples and, overall, less porosity. The $NiO/LaFeO_3$ catalyst has a pore size distribution mainly after 10 nm of pore width, and its pore volume doubles that of $NiO/CaZrO_3$, in accordance with their surface area values.

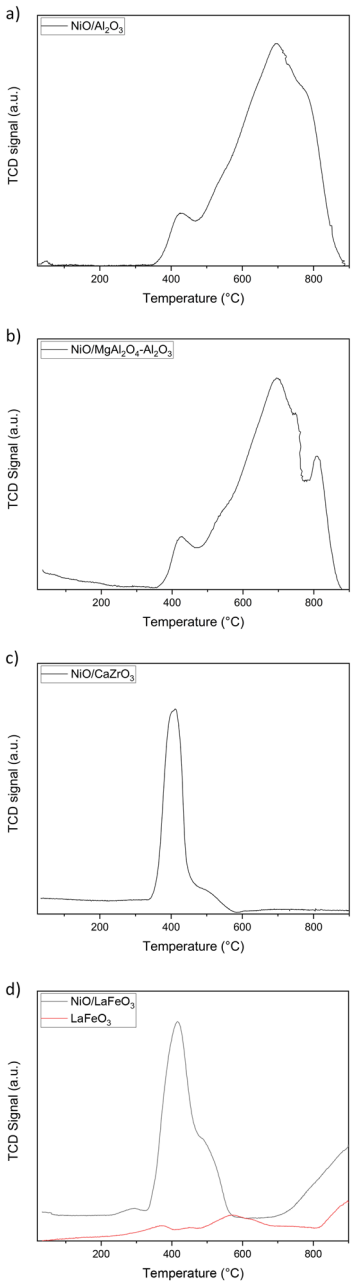

Fig. 2 H_2-TPR experiment on NiO/Al_2O_3 (a), $NiO/MgAl_2O_4$–Al_2O_3 (b), $NiO/CaZrO_3$ (c) and $NiO/LaFeO_3$ (d, black) and $LaFeO_3$ support (d, red) (from room temperature to 900 °C) (H_2 quantification in ESI†).

3.1.3. Study of the reduced catalysts. The calcined catalysts were then studied by H_2-TPR experiments to gain insight into catalyst reducibility and to characterize Ni species and their reduction degrees in the samples (Fig. 2). After H_2-TPR, XRD analysis was made to observe the crystalline phases present in the post reduction samples, as shown in Fig. 3, together with the pre-reduction catalysts to appreciate the differences after the reduction treatment. Moreover, Ni dispersion in the reduced catalysts was evaluated *via* H_2-pulsed chemisorption.

NiO/γ-Al_2O_3 exhibited 2 reduction peaks at 400 °C and 700 °C (Fig. 2(a)). The first reduction peak is attributed to NiO weakly interacting with γ-Al_2O_3, while the second peak at higher temperatures is attributed to a strong interaction between nickel and alumina.[39] The latter has a shoulder above 700 °C probably due to $NiAl_2O_4$ spinel, as reported in

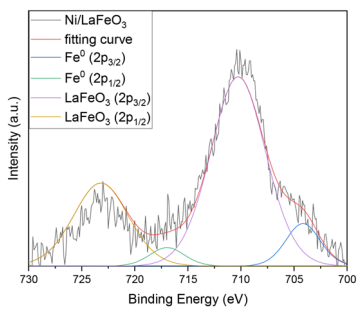

Fig. 3 Detailed XPS spectra of Fe 2p photopeak for $Ni/LaFeO_3$ catalyst (after H_2-TPR from room temperature to 600 °C).

the literature.[19,40,41] Therefore, γ-Al_2O_3 is prone to the formation of the nickel spinel, as at high calcination temperatures, nickel ions gain sufficient energy to integrate into the alumina lattice to produce the spinel.[19]

For NiO/$MgAl_2O_4$–Al_2O_3 (Fig. 2(b)), a first peak was detected at around 400 °C due to surface NiO weakly interacting with $MgAl_2O_4$ for the previous catalyst. The second and third peaks were detected at 700 °C and 800 °C, respectively. The second peak is broad and has a left shoulder above 600 °C and a right shoulder around 746 °C, suggesting different strengths of interaction. High reduction temperatures are usually attributed to spinel strongly interacting with nickel particles, so most probably at 800 °C, nickel enters the magnesium aluminum spinel to form the nickel aluminum spinel.[42,43] To investigate this possibility, the XRD of the reduced sample was analyzed, as shown in Fig. 3(b). Perovskite samples showed reducibility at low temperatures (400 °C), corresponding to NiO weakly interacting with the perovskite support (Fig. 2(c) and (d)). In NiO/$LaFeO_3$ (Fig. 2(d)), an additional peak was observed from 750 °C, which accounts for perovskite reduction, as confirmed by the literature and XRD analysis (Fig. 3(d)).[44] To verify whether $LaFeO_3$ reduction occurred in correspondence with NiO reduction, an additional H_2-TPR experiment was performed on the perovskite support (Fig. 2(d)); this allowed us to verify the reduction of perovskite at 750 °C and to appreciate the reduction process at 400–600 °C, giving iron sub-stoichiometric perovskites, as reported in the literature.[45]

XRD patterns of the reduced catalysts were collected and are shown in ESI† (Fig. S3). Complete reduction of NiO to Ni^0 was observed for all catalysts. For alumina-based catalysts, however, Ni^{II} present as $NiAl_2O_4$ could be reduced to Ni^0. No information could be retrieved about the presence or reduction of $NiAl_2O_4$ spinel in NiO/Al_2O_3 (Fig. S3(a)†) due to the overlap of its peak with Ni, NiO and Al_2O_3 peaks; therefore, further analysis was performed (see XPS analysis, subsubsection 3.1.4.). However, the XRD pattern of the post-calcination and post-reduction NiO/$MgAl_2O_4$–Al_2O_3 catalyst (Fig. S3(b)†) showed differences in the peak at $2\theta = 66°$. The broad peak is symmetric in NiO/$MgAl_2O_4$–Al_2O_3, with contributions of $MgAl_2O_4$, Al_2O_3 and possibly $NiAl_2O_4$ reflections. When the catalyst is reduced, a significant change in the shape of the peak can be observed, which accounts for the loss of a contribution to its left shoulder. At this 2θ, the latter contribution is most probably due to the presence of the spinel, which can be reduced (totally or partially) during reductive treatment to gain the active metallic phase of the catalyst. The spinel peaks overlap with $MgAl_2O_4$ and Al_2O_3 peaks; therefore, XPS analysis was performed to verify this hypothesis (subsubsection 3.1.4.). Besides, XRD analysis shows a complete reduction of crystalline NiO to Ni. XRD of post-reduction perovskite samples showed the complete reduction of NiO as in the previous samples (Fig. S3(c) and (d)†). NiO/$LaFeO_3$ showed La_2O_3 and metallic Fe formation due to perovskite reduction, as expected from the literature (Fig. S3(d)†).[45]

Moreover, an additional H_2-TPR treatment from room temperature to 600 °C of NiO/$LaFeO_3$ was done to verify the complete reduction of NiO. XRD analysis allowed us to observe the complete reduction of NiO to its active form (Fig. S3(e)†), while the presence of Fe^0 given by the formation of iron sub-stoichiometric perovskites was confirmed by XPS analysis, where Fe^0 presence is evidenced by a contribution at 707 eV to $LaFeO_3$ $2p_{3/2}$ (Fig. 3).[36,46]

H_2-pulsed chemisorption was conducted on all catalysts to determine nickel dispersion after reduction, using Bartholomew approximation.[47] Ni dispersion (reported in ESI†) was approximately 0.3% for all samples except for Ni/$CaZrO_3$, for which the value of 1.66% could not be rationalized with the other characterization results (H_2-TPR, XRD, XPS and TEM data), thereby implying a mismatch with the reference model assumptions (such as having spherical particles, having 1 hydrogen atom adsorbed by

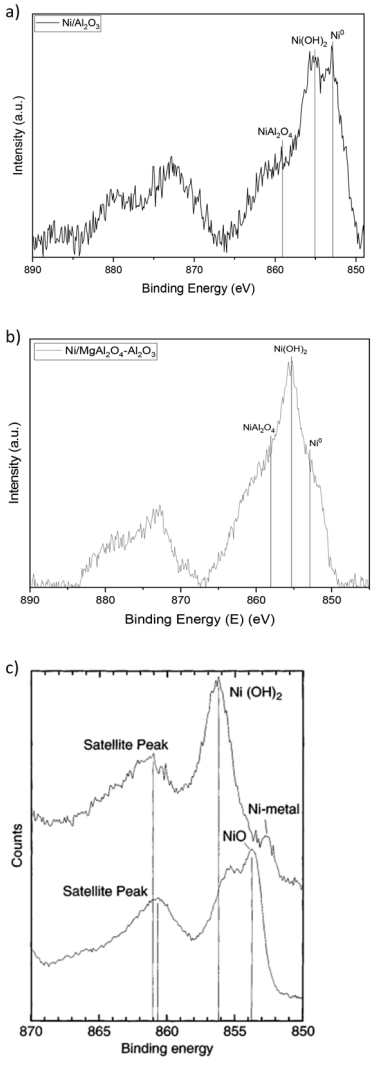

Fig. 4 Detailed XPS spectra of Ni 2p photopeak for Ni/Al_2O_3 (a) and Ni/$MgAl_2O_4$–Al_2O_3 (b) samples (post H_2-TPR) and reference spectra of Ni, $Ni(OH)_2$ and NiO taken from the literature (c).[48] Ni 2p fit is available in ESI.†

each nickel atom and having only hydrogen chemisorption due to the nickel present in the samples). The dispersion was correlated with the strength of the interaction of Ni particles with the support (see H_2-TPR above). For Ni/$MgAl_2O_4$–Al_2O_3 characterized by the strongest interaction with Ni, a higher dispersion value was found (0.36%), while Ni/$LaFeO_3$ had the lowest dispersion (0.26%) due to the low interaction of Ni with the support. Ni dispersion was further analyzed using TEM (Fig. S4†), which showed for alumina-based samples similar Ni distribution, with particle dimensions in the range of 15–20 nm. Perovskite samples showed less dispersed Ni due to their low surface area (see Table 1). On Ni/$CaZrO_3$, a very large conglomerate and inhomogeneous Ni distribution for Ni/$LaFeO_3$, an intricate pattern was found, which revealed the presence of Ni particles with dimensions around 8–16 nm at the edges of the fragments, while at the core of the fragments, conglomeration of the latter nanoparticles was expected due to the lower interaction with the support and the lowest Ni dispersion (see above). Therefore, TEM allowed us to conclude that while alumina-based catalysts had a good distribution of Ni particles, perovskite's low area caused the formation of agglomerations of Ni nanoparticles, especially for Ni/$CaZrO_3$.

3.1.4. Study on the active catalysts: XPS results. First, XPS detailed spectra of Ni2p were acquired for reduced alumina-based catalysts to investigate the possible presence of nickel spinel after the reduction treatment (Fig. 4).

From the Ni 2p photopeak, it is possible to observe the presence of two contributions: Ni^0 at 852.9 eV, as expected after the reduction treatment, and a Ni^{II} species contribution at 855.3 eV. The latter species was attributed to nickel hydroxide, as expected for impregnated nickel nanoparticles exposed to air after reduction.[49] The presence of this species is probably due to metallic nickel that is superficially oxidized when placed in contact with air; this explains why $Ni(OH)_2$ is visible in XPS spectra (Fig. 4) and not in XRD measurements (Fig. S3†), as only the most superficial layers of Ni^0 are oxidized. However, this phenomenon does not affect the catalytic activity of the samples, as catalysts are reduced and then directly tested for catalytic activity using the same apparatus, thereby avoiding the oxygen-containing atmosphere of the air.

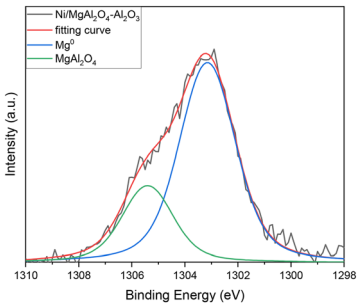

Fig. 6 Detailed XPS spectra of Mg 1s photopeak for Ni/$MgAl_2O_4$–Al_2O_3 catalyst (post H_2-TPR) and its fit.

By comparing the Ni photopeak of alumina-based catalysts (Fig. 4(a) and (b)) with the reference peak (Fig. 4(c)), an added contribution can be observed in the spectra. This contribution can be centered around 858.1 eV, and it accounts for the presence of a Ni^{II} species different from $Ni(OH)_2$, which is in agreement with what is expected for this element in $NiAl_2O_4$ spinel. To verify this hypothesis, Al 2p photopeaks were acquired and revealed the presence of the spinel (Fig. 5(a) and (b)).

Spinel's contribution can be easily observed in the NiO/Al_2O_3 sample (Fig. 5(a)) owing to the shoulder at 74.7 eV, which accounts for $NiAl_2O_4$ presence in addition to the 74.0 eV peak of Al_2O_3.[50] In NiO/$MgAl_2O_4$–Al_2O_3, a broad peak was detected due to three contributions (Fig. 5(b)): $MgAl_2O_4$ on the left shoulder (75.3 eV), Al_2O_3 on the right

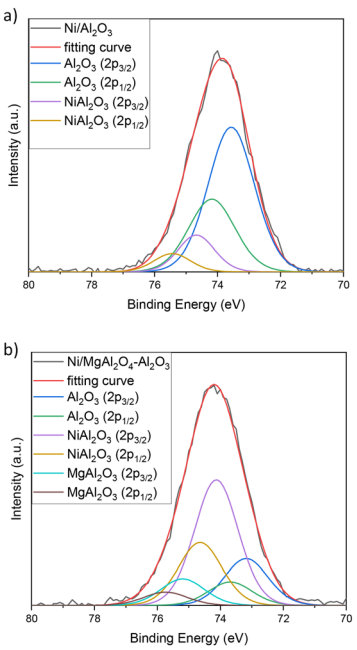

Fig. 5 Detailed XPS spectra of Al 2p photopeak for Ni/Al_2O_3 (a) and Ni/$MgAl_2O_4$–Al_2O_3 (b) catalysts (post H_2-TPR) and their fit.

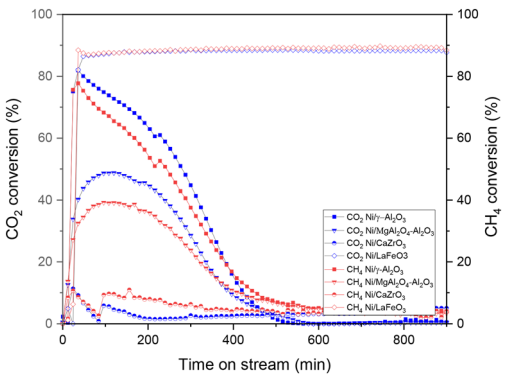

Fig. 7 CO_2 and CH_4 conversions for 5% CH_4, 5% CO_2, 1% NO gas mixture for NiO/Al_2O_3, NiO/$MgAl_2O_4$–Al_2O_3, NiO/$CaZrO_3$ and NiO/$LaFeO_3$ catalysts.

side of the peak (74.0 eV) and a last contribution on the left of the peak at 74.7 eV attributed to $NiAl_2O_4$ spinel.[36,51] To gain more information about the species present in the sample, a Mg 1s photopeak was acquired (Fig. 6).

$MgAl_2O_4$ was present at 1305.5 eV, and another contribution at 1303 eV was attributed to Mg^0. This species could form due to the entry of Ni into the $MgAl_2O_4$ structure, causing the formation of the spinel $NiAl_2O_4$ and the reduction of Mg^{2+} that was in the spinel structure to Mg^0. This has been previously observed in the literature for catalysts with high nickel loadings.[52]

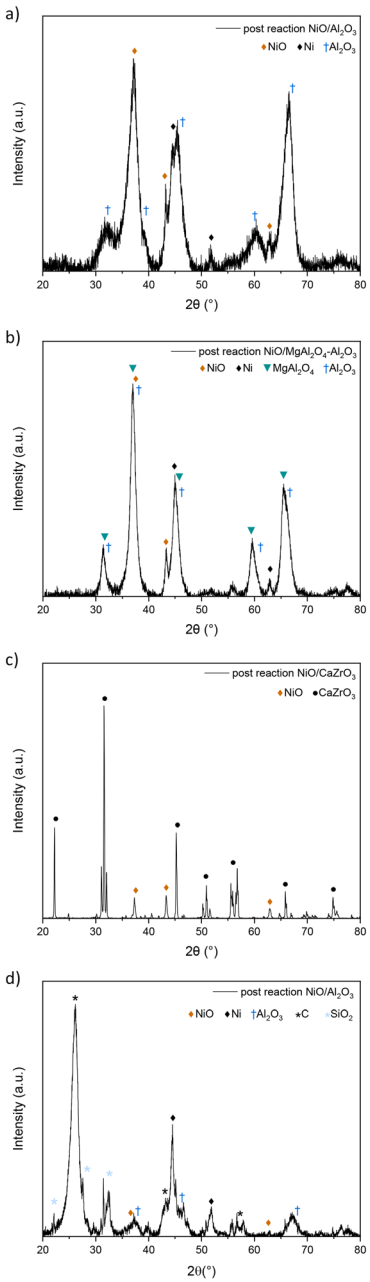

Fig. 8 XRD pattern of post-reaction catalytic experiment on NiO/Al_2O_3 (a), $NiO/MgAl_2O_4$–Al_2O_3 (b), $NiO/CaZrO_3$ (c) and $NiO/LaFeO_3$ (d) catalysts (5% CH_4, 5% CO_2, and 1% NO gas mixture).

3.2. Catalytic performance: impact of the support

3.2.1. Catalytic tests. Catalytic activity was tested for the 4 catalysts by analyzing CO_2 and CH_4 conversions. Tests were performed with two different reaction mixtures, composed of 5% CH_4, 5% CO_2, and 1% NO (Fig. 7) as well as 25% CH_4, 25% CO_2, and 1% NO (Fig. 9) using Ar as a carrier gas for a total flow rate of 100 mL min^{-1}.

The first tests were conducted with a 5% CH_4, 5% CO_2, and 1% NO gas mixture (Fig. 7). All catalysts except $NiO/LaFeO_3$ encountered rapid deactivation in the first 400 minutes of the reaction. Alumina-based catalysts showed high initial conversions, which rapidly went from around 80% and 40% for NiO/Al_2O_3 and $NiO/MgAl_2O_4$–Al_2O_3, respectively, to no catalytic activity after 500 minutes. XRD analysis was performed to understand the cause of deactivation (Fig. 8). No carbon was shown by XRD analysis due to the low concentration of reactants and to the high NO concentration, which enhanced the oxidative properties of the reaction mixture.[7] Moreover, from the XRD patterns of the post-reaction catalysts (Fig. 8), it was possible to observe the strong oxidation of Ni from its active metal form to its inactive oxide form. Nickel conversion to NiO is believed to be a reaction that causes fast catalyst deactivation.[7] Comparing the activity of the alumina-based catalysts, the NiO/Al_2O_3 catalyst showed the highest CO_2 and CH_4 conversions (around 70% in the first 200 minutes of reaction), which decreased by 20% for over 200 minutes, while $NiO/MgAl_2O_4$–Al_2O_3's conversions were lower (around 40%) but remained constant simultaneously. This might be due to the better stability of Ni particles due to their interaction with $MgAl_2O_4$–Al_2O_3 support, as suggested by H_2-TPR studies (subsubsection 3.2.3.). Perovskite catalysts were tested, showing different behaviors from each other. Although $NiO/CaZrO_3$ had almost no catalytic activity (maximum conversion of 10% for both reactants), $NiO/LaFeO_3$ showed the highest and most stable activity, with CO_2 and CH_4 conversions around 90% during all the reaction times. The latter catalyst showed comparable CO_2 and CH_4 conversions that are influenced by a change in NO behavior, while for the other catalysts, NO reacted with Ni until complete NiO oxidation and catalytic activity were retained

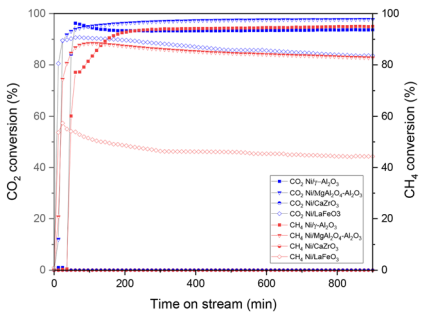

Fig. 9 CO_2 and CH_4 conversions for 25% CH_4, 25% CO_2, and 1% NO gas mixture for NiO/Al_2O_3, $NiO/MgAl_2O_4$–Al_2O_3, $NiO/CaZrO_3$ and $NiO/LaFeO_3$ catalysts.

throughout all 15 hours. This means that NO must react with either CH_4 or another reducing gas produced by dry reforming of methane, such as CO or H_2, to ensure complete NO reduction to N_2, as was observed during the process. Because NiO/$CaZrO_3$'s poor interaction with nickel particles determines its fast deactivation due to NO oxidation, NiO/$LaFeO_3$ was able to protect the particles from NO, and perovskite was able to reduce NO and therefore preserve the nickel particles in their metal form. Overall, $LaFeO_3$ was the best support for these reactant concentrations, providing high catalytic activity (90% CO_2 and CH_4 conversions) throughout the 900 minutes tested. The XRD pattern of post reaction NiO/$LaFeO_3$ (Fig. 8(d)) showed NiO presence. However, nickel in its active metal form must be present to ensure the high and constant catalytic activity obtained; thus, Ni^0 would most probably be present as an amorphous or highly dispersed form in the sample.

As the first tests showed deactivation problems due to nickel oxidation by NO, further tests were performed to achieve a less oxidative environment using a 25% CH_4, 25% CO_2, and 1% NO gas mixture, aiming to balance NO oxidative power with a higher concentration of CH_4 reactant and CO and H_2 produced by DRM reaction (1) (Fig. 9).

High and stable conversions were obtained for NiO/Al_2O_3, which were around 93% for CO_2 and 94% for CH_4. At the beginning of the experiment, high CO_2 conversions were immediately achieved for NiO/Al_2O_3, while CH_4 reached its maximum activity after 200 minutes of reaction probably due to the presence of nickel in a non-active form, such as $NiAl_2O_4$ or Ni, strongly interacting with the support, as previously observed in H_2-TPR studies (subsubsection 3.1.3.). During the reaction, as H_2 develops from the DRM reaction (1), nickel can be reduced in its active metal form. CO_2 conversions, however, slightly decreased until 200 minutes of reaction, passing from around 96% to 93%; this could be explained by a contribution to CO_2 concentrations due to the nitric oxide reaction with coke (reaction (5)), which gives CO_2 as a product, therefore causing higher CO_2 concentrations in the reaction mixture. The XRD pattern of the spent catalyst (Fig. 10(a)) showed a relevant carbon deposition in the form of graphite. Ni is present in its active metallic form. Little NiO is present in the pattern although it does not cause problems to the catalytic activity, as can be deduced from the stability of the conversions. γ-Al_2O_3 support was not modified during the reaction; $NiAl_2O_4$ spinel was not detected by XRD analysis probably because during the reaction, part of H_2 can reduce Ni^{II} of $NiAl_2O_4$ to its metallic form.[53]

NiO/$MgAl_2O_4$–Al_2O_3 showed high CO_2 and CH_4 conversions (97% and around 85% respectively), with CO_2 conversion higher than CH_4 probably due to the basicity of the support that enhances CO_2 adsorption, therefore leading to the reverse water gas shift reaction (2).[54,55] CO_2 conversions were stable; however, CH_4 conversion decreased slightly in 15 hours, decreasing from around 88% to 82%. This might be due to deactivation that occurs during the reaction as a result of sintering and coking, which could diminish the number of active sites in the samples, which affects NiO/$MgAl_2O_4$–Al_2O_3 and not NiO/Al_2O_3 due to the different surface area values (see Table 1). The XRD pattern (Fig. 10(b)) revealed the presence of graphitic carbon as in the previous sample; nickel was present in its metallic form, and no nickel oxide was detected probably because of the high interaction between the support and Ni particles previously determined by H_2-TPR (subsubsection 3.1.3.).

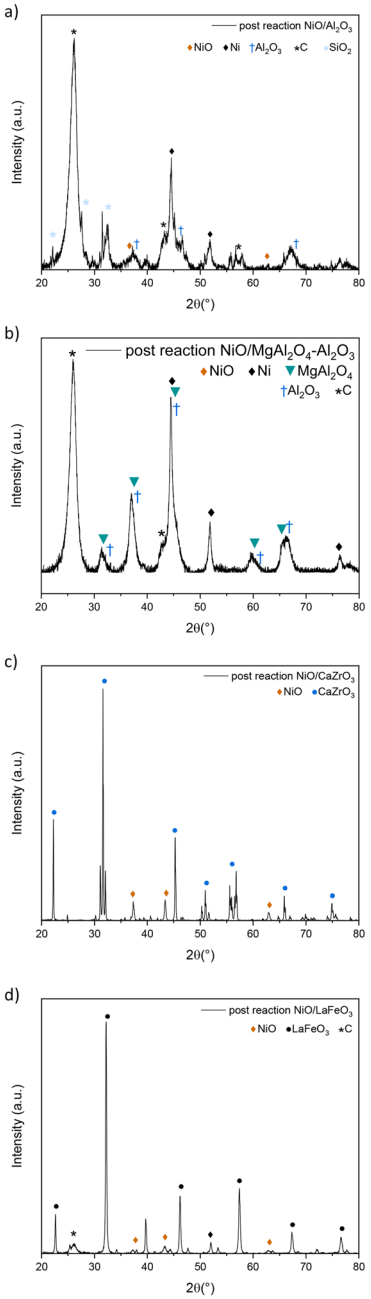

Fig. 10 XRD pattern of post-reaction experiment on NiO/Al_2O_3 (a), NiO/$MgAl_2O_4$–Al_2O_3 (b), NiO/$CaZrO_3$ (c) and NiO/$LaFeO_3$ (d) catalysts (25% CH_4, 25% CO_2, and 1% NO gas mixture).

No nickel spinel was detected, which was probably reduced by H_2 produced in the process as for NiO/Al_2O_3, while the support remained unchanged for the rest.

$NiO/CaZrO_3$ showed no catalytic activity (Fig. 9), and post-reaction XRD showed complete nickel oxidation (Fig. 10(c)). This is likely due to the perovskite support, with its low interaction with Ni particles, as observed in H_2-TPR (subsubsection 3.1.3.), could not protect the Ni particles from NO oxidation, and Ni agglomeration occurred because of the low surface area (see Table 1 and SEM-EDX maps). Therefore, no carbon was deposited during the process, as nickel was deactivated by oxidation before carbon deposition occurred (Fig. 10(c)).

$NiO/LaFeO_3$ sample showed high CO_2 conversion (around 91%) at the beginning of the reaction, which then diminished until 83% at the end of the process (Fig. 9). CH_4 conversions started at 55% and then decreased to 44% (Fig. 9). For this catalyst, it is interesting to compare the conversions between the 5% CO_2, 5% CH_4, and 1% NO (Fig. 7) as well as the 25% CO_2, 25% CH_4, and 1% NO tests (Fig. 9). Comparing the activity recorded in this test and the one with 1/5 of CO_2 and CH_4 reactant, it appears that the catalyst does not have the same stability of conversions in the range of time as in the previous test. Conversions slowly decreased over time probably owing to the weaker interaction of nickel particles with the perovskite support (see subsubsection 3.1.3.), which caused Ni particles to be more sensitive to sintering and coking during the reaction, leading therefore to a slow deactivation.[56] It is also important to remember that perovskite-based catalysts are characterized by low surface area values (1 order of magnitude difference from alumina-based samples (see section 3.1.2.)) that can have an impact on the catalytic behaviour of the sample. In 5% CO_2, 5% CH_4 and 1% NO tests (Fig. 7), the conversions were constant in the reaction time because no coke was deposited, therefore limiting the deactivation due to coke deposition, and the properties of the supports allowed the particles to be protected from NO oxidation, as observed before.[18] Post-reaction XRD (Fig. 10(d)) showed the presence of graphitic carbon and partial nickel oxidation to NiO as in the other samples; the support remained unchanged during the 15 hour process.

Finally, TOF values were calculated for both CO_2 and CH_4 to compare catalyst reactivity under the two different conditions (see ESI†).[57] However, we consider that both CO_2 and CH_4 are involved in side reactions (see the Introduction). Therefore, CO_2 and CH_4 conversions employed for TOF calculations contribute owing not only to the dry reforming of methane but also to carbon deposition, its gasification with CO_2, and RWGS. TOF values followed the trend of reactant conversions and increased by 1 order of magnitude for 25% CO_2/CH_4 tests due to the increased quantity of fluxed reactants and the higher conversions obtained owing to the more balanced reducing/oxidative gas mixture.

3.2.2. Effect of the support on carbon deposition. XPS was performed on post-reaction samples to gain information about the coke produced in 25% CO_2, 25% CH_4, and 1% NO tests. In Table 2, the calculated values of carbon surface compositions are reported and compared for the post-reduction and post-reaction catalysts.

As expected, carbon atomic percentage drastically increases after catalysis for all samples except $NiO/CaZrO_3$, which had no catalytic activity (Fig. 9 and 10) and in which the carbon amount decreases presumably as a consequence of thermal treatment. Regarding alumina-based catalysts, post-reaction catalysts have a higher carbon surface composition for acidic supported catalyst NiO/Al_2O_3 than for basic catalyst $NiO/MgAl_2O_4–Al_2O_3$, as expected for the improved CO_2 chemisorption enhancement typical of basic supports.[12] Moreover, post-reaction $NiO/LaFeO_3$ shows the lowest concentration of carbon on its surface better than $NiO/MgAl_2O_4–Al_2O_3$; this could be related to its ability to interact with NO molecules and therefore facilitate the NO gasification of coke.[28]

To better understand the coking phenomena, detailed C1s XPS spectra of the post-reaction catalysts were acquired, as shown in Fig. 11.

C1s photopeaks of $CaZrO_3$ showed typical features of adventitious carbon C–C peak at 284.8 eV, and at higher binding energies typical C–O–C (286 eV) and O–C═O (288.5 eV) contributions were observed. Carbonate species were also present on the $NiO/MgAl_2O_4–Al_2O_3$ catalyst, which is consistent with the mentioned hypothesis of enhanced capability of interaction with CO_2 and consequent lower coke poisoning. For NiO/Al_2O_3, $NiO/MgAl_2O_4–Al_2O_3$ and $NiO/LaFeO_3$ catalysts, the peak was centered at 284.5 eV, a typical value for the C–C bond of the graphitic carbon. A tail can be observed around 285–286 eV, which accounts for satellites of C1s.[36,58] Moreover, in $NiO/MgAl_2O_4–Al_2O_3$, it is possible to appreciate an additional contribution at around 286 eV due to oxygenating species that are present together with the adventitious carbon peak.[59] Therefore, XPS results confirm the presence of graphitic carbon obtained through XRD experiments (Fig. 10).

Table 2 XPS (5–10 nm depth) elemental quantifications for *C* calculated for post-reduction and post-reaction samples (surveys available in ESI†)

Support	Post-reduction *C* atomic surface composition (at%)	Post-reaction *C* atomic surface composition (at%)
Al_2O_3	26.0	89.3
$MgAl_2O_4–Al_2O_3$	8.6	85.9
$CaZrO_3$	28.9	15.1
$LaFeO_3$	31.4	82.9

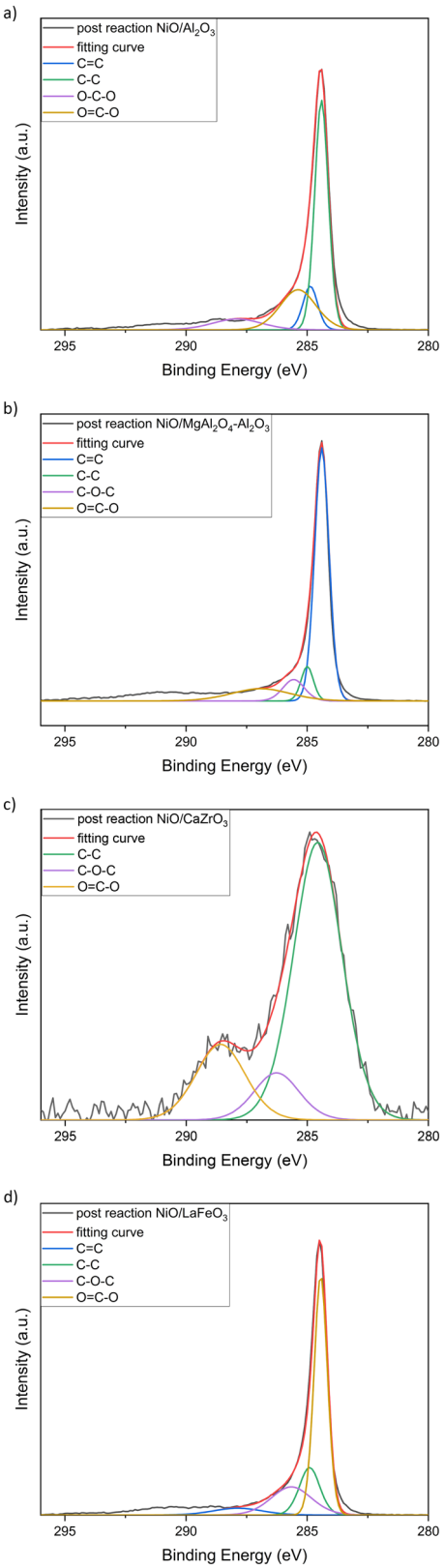

Fig. 11 XPS spectra for C 1s of post-reaction samples (25% CH_4, 25% CO_2, and 1% NO gas mixture) for NiO/Al_2O_3 (a), $NiO/MgAl_2O_4$–Al_2O_3 (b), $NiO/CaZrO_3$ (c) and $NiO/LaFeO_3$ (d) catalysts.

Raman spectroscopy (Fig. S7†) was then performed, and the XPS results were confirmed. Both catalysts showed typical

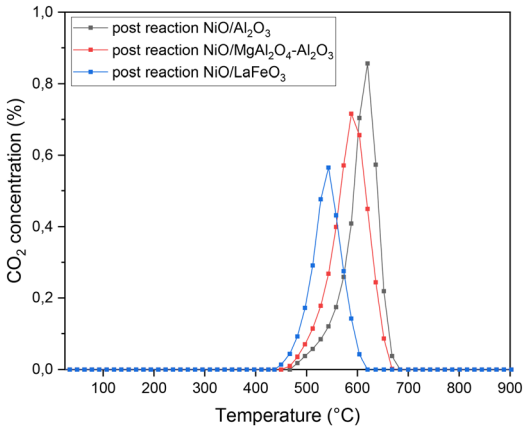

Fig. 12 CO_2 conversions *vs.* temperature results for O_2-TPO experiments conducted on post-reaction samples: NiO/Al_2O_3, $NiO/MgAl_2O_4$–Al_2O_3 and $NiO/LaFeO_3$ catalysts.

D and G vibration bands of carbon materials linked to defects or the disordered carbon (D-band, 1350 cm^{-1}) and to C=C stretching vibration of sp^2 of the graphitic carbon (G-band 1580 cm^{-1}). Combination bands (D + G and 2D) can also be observed in the second part of the spectrum.[18,60]

Finally, post-reaction catalysts undergo O_2-TPO to determine the type of carbon deposited during the catalytic reaction (Fig. 12). As observed by various authors, the temperature at which coke reacts with oxygen and the quantity of carbon dioxide produced can provide useful information about the type and amount of deposited carbon.[30,61–63]

A 5% O_2 gas stream was fed onto the post-reaction catalysts, heated from around room temperature (25 °C) until 900 °C, resulting in the gasification of coke starting above 400 °C, with CO_2 developed from the coke reaction with oxygen.[64] Coke was gasified between 450 °C and 700 °C, which is the temperature range corresponding to the gasification of graphitic carbon, as expected from XRD (Fig. 10) and XPS results (Fig. 11).[64] When comparing the temperature range where CO_2 was detected (Fig. 12), it can be observed that NiO/Al_2O_3 developed CO_2 mainly after 625 °C, therefore at higher temperatures compared to the basic catalyst $NiO/MgAl_2O_4$–Al_2O_3, with CO_2 peak centred around 580 °C. Indeed, a trend between the basicity of the support and the reactivity of the deposited carbon can be observed, as expected from the literature, due to the interaction between the support and CO_2 acidic molecule.[65] $NiO/LaFeO_3$ showed the lowest gasification temperatures, allowing the majority of carbon to be gasified at around 530 °C; this could be due to a difference in carbon reactivity favoured by the better interaction between NO and the catalyst favoured by $LaFeO_3$ support, as later explained (Fig. 13).[18,64] Additionally, the amount of CO_2 developed on the different catalysts in O_2-TPO tests was compared, as presented in Table 3.

It can be observed that the amount of CO_2 produced, *i.e.* of carbon gasified, does not follow the same trend as the

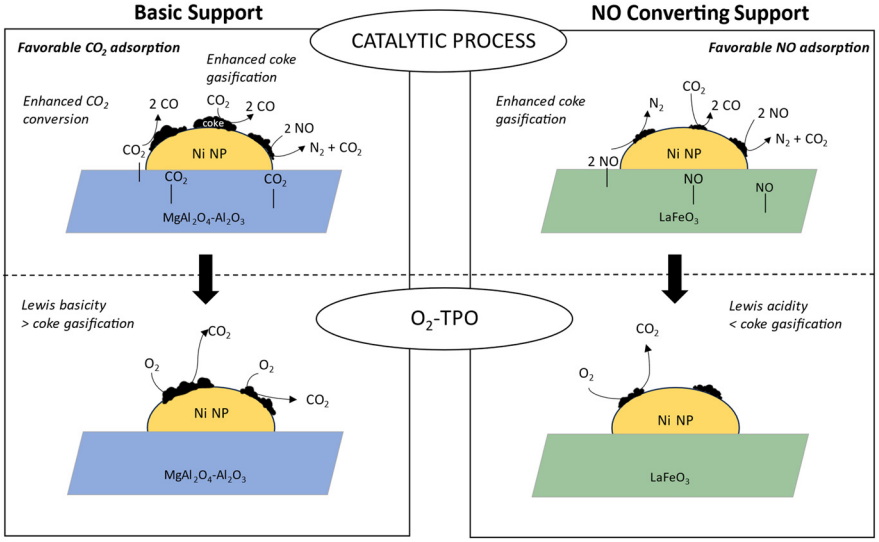

Fig. 13 Graphical scheme to represent the impact of the properties of the support in coke deposition and gasification during the course of the process (DRM coupled with NO reduction, shown in the upper part) and during O_2-TPO experiments (study on coke's reactivity, shown in the lower part). In particular, the effect of having Lewis basicity is shown on the left of the figure owing to the $MgAl_2O_4$ coating, while NO adsorption ability is shown on the right owing to the $LaFeO_3$ support.

Table 3 Comparison of coke deposited on post-reaction catalysts analyzed through gasification *via* O_2-TPO and XPS analysis

Support	O_2-TPO gasified coke (wt%)	XPS analyzed (at%)	XPS analyzed coke (wt%)
Al_2O_3	57.2	89.3	0.8
$MgAl_2O_4$–Al_2O_3	61.1	85.9	0.7
$LaFeO_3$	41.1	82.9	0.5

quantity of carbon determined by XPS analysis on post-reaction catalysts (Table 3). This can be explained by the difference in reactivity due to the support, which can influence the interaction of carbon species with the gases of the mixture; the acidic/basic properties of the support can influence CO_2 interaction with the surface and therefore coke gasification, as well as NO that can differently impact the catalysts based on the support choice, as has been observed for nickel particles oxidized in the catalytic experiments, which strongly depended on the support interaction with NO (subsubsection 3.1.5.).[66,67] The effects of these properties on the catalytic activity and O_2-TPO experiments are depicted in Fig. 12. Supports with Lewis basicity or NO conversion ability tend to have less coke because during the reaction, coke can be gasified by interacting with either the adsorbed CO_2 *via* the reverse Boudouard reaction (4) or by reacting with NO (reaction (5)), therefore explaining the lower quantities of carbon detected by XPS analysis ($MgAl_2O_4$–Al_2O_3 85.9 at%, $LaFeO_3$ 82.9 at% < Al_2O_3 89.3 at%). In O_2-TPO experiments, the wt% of gasified coke was influenced not only by the overall quantity of coke present on the catalysts (*i.e.* XPS results) but also by the reactivity of the carbon deposited during the process, which affects the ability of the support to interact with the different gases of the mixture. This could explain why Al_2O_3 showed more coke gasification than $LaFeO_3$ (Al_2O_3 57.2 wt% > $LaFeO_3$ 41.1 wt%), being the support that allowed for the highest carbon deposition during the process (Al_2O_3 89.3 at%); however, the $MgAl_2O_4$–Al_2O_3-supported catalyst showed the highest amount of gasified carbon ($MgAl_2O_4$–Al_2O_3 61.1 wt%), which could be due to a more reactive carbon deposited during the process, given by the interaction of coke with the CO_2 adsorbed by the Lewis basic sites.[68]

Conclusions

In this work, a recent strategy was studied in which DRM and nitric oxide reduction occurred simultaneously in the reactor, with the aim of addressing the carbon deposition problem and the consequent deactivation that is typical of Ni-based catalysts in DRM.

In particular, this study effectively shows the role of the support in this process and how the support's properties deeply influence the catalytic activity and stability of the catalysts. Among the four different supports that were tested, high and stable catalytic activity was achieved when the support could help protect nickel nanoparticles from NO oxidation and, if coking occurred, when the support had enough surface area to avoid the blockage of the active sites. In the 5% CO_2, 5% CH_4, and 1% NO tests, the high relative NO content in the gas mixture caused the oxidation of nickel in its active metal form in all catalysts. Only NiO/$LaFeO_3$ could have high and stable conversions of reactants (90%) due to its ability to convert NO reaching the catalyst surface, thereby protecting Ni particles from oxidation. NO oxidative properties were balanced in 25% CO_2, 25% CH_4, and 1% NO

gas mixture, where the required properties of the support changed: the support here required both a high surface area to prevent coking phenomena to block the catalyst active sites, and a high interaction between the active phase and the support to prevent Ni oxidation.

Therefore, high and stable conversions were achieved in 900 minutes of flow for NiO/γ-Al_2O_3, which exhibited around 93% for CO_2 conversions and 94% for CH_4 conversions, owing to both its high specific surface area (104.7 m^2 g^{-1}) and the interaction between metal particles and the support, which allowed for good Ni dispersion (SEM-EDX maps). Complete NO conversion was effectively obtained under both tested conditions, therefore diminishing the amount of coke deposited and allowing for complete NO conversion without the use of valuable resources (such as NH_3 in selective reduction of nitric oxide). Therefore, this process is an interesting solution for improving the energetic efficiency of pollutant conversions in post-production industrial plants, with the properties of the supports that need to be tuned based on the oxidative/reductive properties of the gas compositions.

Data availability

The data supporting this article have been included as part of the ESI.†

Author contributions

Beatrice Senoner: conceptualization, investigation, methodology, validation, visualization, writing – original draft; Andrea Osti: investigation, methodology, project administration, supervision, writing – review and editing; Antonella Glisenti: investigation, funding acquisition, project administration, resources, supervision, writing – review and editing.

Conflicts of interest

There are no conflicts to declare.

Acknowledgements

The authors acknowledge the financial support of the European Union's KNOWSKITE-X project under grant agreement No. 101091534 for the provision of funding. The authors would also like to thank CNR (Consiglio Nazionale delle Ricerche) for the funding of XPS set-up funded by "Sviluppo delle infrastrutture e programma biennale degli interventi del Consiglio Nazionale delle Ricerche (2019)".

Notes and references

1 Y. Lu, D. Guo, Y. Zhao, Y. Zhao, S. Wang and X. Ma, *Appl. Catal., B*, 2021, **291**, 120075.
2 J. Deng, B. Yang, Y. Liu, X. Zhang, J. Zheng and D. Zhang, *Appl. Catal., A*, 2022, **642**, 118706.
3 N. Hadian and M. Rezaei, *Fuel*, 2013, **113**, 571–579.
4 I. V. Yentekakis, P. Panagiotopoulou and G. Artemakis, *Appl. Catal., B*, 2021, **296**, 120210.
5 M. Tao, X. Meng, Y. Lv, Z. Bian and Z. Xin, *Fuel*, 2016, **165**, 289–297.
6 T. Juzsakova, N. Al-Jammal, I. Cretescu, V. Sebestyén, C. Le Phuoc, E. Domokos, Á. Rédey and C. D. Stan, *Minerals*, 2018, **8**, 462.
7 J. Hu, V. V. Galvita, H. Poelman, Z. Wang, G. B. Marin and S. Kawi, *Appl. Catal., B*, 2021, **297**, 120472.
8 F. Gholami, M. Tomas, Z. Gholami and M. Vakili, *Sci. Total Environ.*, 2020, **714**, 136712.
9 T. Andana, K. G. Rappé, F. Gao, J. Szanyi, X. Pereira-Hernandez and Y. Wang, *Appl. Catal., B*, 2021, **291**, 120054.
10 R. Mrad, A. Aissat, R. Cousin, D. Courcot and S. Siffert, *Appl. Catal., A*, 2015, **504**, 542–548.
11 B. Guan, R. Zhan, H. Lin and Z. Huang, *Appl. Therm. Eng.*, 2014, **66**, 395–414.
12 A. Abdulrasheed, A. A. Jalil, Y. Gambo, M. Ibrahim, H. U. Hambali and M. Y. Shahul Hamid, *Renewable Sustainable Energy Rev.*, 2019, **108**, 175–193.
13 X.-H. Pham, U. P. M. Ashik, J.-I. Hayashi, A. Pérez Alonso, D. Pla, M. Gómez and D. Pham Minh, *Appl. Catal., A*, 2021, **623**, 118286.
14 T. Wei, L. Jia, J.-L. Luo, B. Chi, J. Pu and J. Li, *Appl. Surf. Sci.*, 2020, **506**, 144699.
15 F. S. Al-Mubaddel, R. Kumar, M. L. Sofiu, F. Frusteri, A. A. Ibrahim, V. K. Srivastava, S. O. Kasim, A. H. Fakeeha, A. E. Abasaeed, A. I. Osman and A. S. Al-Fatesh, *Int. J. Hydrogen Energy*, 2021, **46**, 14225–14235.
16 M. F. Zawrah, H. Hamaad and S. Meky, *Ceram. Int.*, 2007, **33**, 969–978.
17 S. Dama, S. R. Ghodke, R. Bobade, H. R. Gurav and S. Chilukuri, *Appl. Catal., B*, 2018, **224**, 146–158.
18 M. Yang, Y. Wang, R. Zhang, T. Liu, L. Xia, Z. Chen, X. Fang, X. Xu, J. Xu and X. Wang, *Catal. Surv. Asia*, 2021, **25**, 424–436.
19 L. Zhou, L. Li, N. Wei, J. Li and J.-M. Basset, *ChemCatChem*, 2015, **7**, 2508–2516.
20 J. Guo, H. Lou, H. Zhao, D. Chai and X. Zheng, *Appl. Catal., A*, 2004, **273**, 75–82.
21 P. J. Chupas, K. W. Chapman and G. J. Halder, *J. Am. Chem. Soc.*, 2011, **133**, 8522–8524.
22 M. Abbas, U. Sikander, M. T. Mehran and S. H. Kim, *Catal. Today*, 2022, **403**, 74–85.
23 Y. Chen, M. Li, Z. Li, F. Liu, G. Song and S. Kawi, *Energy Convers. Manage.*, 2022, **265**, 115744.
24 M. A. Peña and J. L. G. Fierro, *Chem. Rev.*, 2001, **101**, 1981–2018.
25 S. Bhattar, Md. A. Abedin, S. Kanitkar and J. J. Spivey, *Catal. Today*, 2021, **365**, 2–23.
26 H. R. Radfarnia and M. C. Iliuta, *Chem. Eng. Process.: Process Intesif.*, 2014, **86**, 96–103.
27 E. P. Sari, K. Wijaya, W. Trisunaryanti, A. Syoufian, H. Hasanudin and W. D. Saputri, *Int. J. Energy Environ. Eng.*, 2022, **13**, 967–978.

28 J. Chen, M. Shen, X. Wang, J. Wang, Y. Su and Z. Zhao, *Catal. Commun.*, 2013, **37**, 105–108.
29 N. A. K. Aramouni, J. G. Touma, B. A. Tarboush, J. Zeaiter and M. N. Ahmad, *Renewable Sustainable Energy Rev.*, 2018, **82**, 2570–2585.
30 Z. Alipour, M. Rezaei and F. Meshkani, *J. Energy Chem.*, 2014, **23**, 633–638.
31 F. Meshkani, M. Rezaei and M. Andache, *J. Ind. Eng. Chem.*, 2014, **20**, 1251–1260.
32 A. Osti, L. Rizzato, J. Cavazzani and A. Glisenti, *Catalysts*, 2023, **13**, 1177.
33 L. Rizzato, J. Cavazzani, A. Osti, M. Scavini and A. Glisenti, *Catalysts*, 2023, **13**, 1377.
34 D. A. Shirley, *Phys. Rev. B: Solid State*, 1972, **5**, 4709–4714.
35 J. F. Moulder, W. F. Stickle, P. E. Sobol and K. D. Bomben, *Handbook of X-ray Photoelectron Spectroscopy*, Physical Electronic Division, 1992.
36 *NIST X-ray Photoelectron Spectroscopy Database, NIST Standard Reference Database Number 20*, National Institute of Standards and Technology, Gaithersburg MD, 20899, 2000, DOI: **10.18434/T4T88K**.
37 V. Singh, S. Watanabe, T. K. Gundu Rao, K. Al-Shamery, M. Haase and Y.-D. Jho, *J. Lumin.*, 2012, **132**, 2036–2042.
38 M. Thommes, K. Kaneko, A. V. Neimark, J. P. Olivier, F. Rodriguez-Reinoso, J. Rouquerol and K. S. W. Sing, *Pure Appl. Chem.*, 2015, **87**, 1051–1069.
39 N. F. P. Ribeiro, R. C. R. Neto, S. F. Moya, M. M. V. M. Souza and M. Schmal, *Int. J. Hydrogen Energy*, 2010, **35**, 11725–11732.
40 G. Li, L. Hu and J. M. Hill, *Appl. Catal., A*, 2006, **301**, 16–24.
41 G. Wang, F. Luo, K. Cao, Y. Zhang, J. Li, F. Zhao, R. Chen and J. Hong, *Energy Technol.*, 2019, **7**, 1800359.
42 P. K. Chaudhary, N. Koshta and G. Deo, *Int. J. Hydrogen Energy*, 2020, **45**, 4490–4500.
43 L. Azancot, L. F. Bobadilla, M. A. Centeno and J. A. Odriozola, *J. CO2 Util.*, 2021, **52**, 101681.
44 M. Mokhtar, A. Medkhali, K. Narasimharao and S. Basahel, *J. Membr. Sep. Technol.*, 2014, **3**, 206–212.
45 A. Schön, C. Dujardin, J.-P. Dacquin and P. Granger, *Catal. Today*, 2015, **258**, 543–548.
46 S. Wu, Y. Lin, C. Yang, C. Du, Q. Teng, Y. Ma, D. Zhang, L. Nie and Y. Zhong, *Chemosphere*, 2019, **237**, 124478.
47 C. H. Bartholomew and R. B. Pannell, *J. Catal.*, 1980, **65**, 390–401.
48 H. W. Nesbitt, D. Legrand and G. M. Bancroft, *Phys. Chem. Miner.*, 2000, **27**, 357–366.
49 J. K. Kesavan, I. Luisetto, S. Tuti, C. Meneghini, G. Iucci, C. Battocchio, S. Mobilio, S. Casciardi and R. Sisto, *J. CO2 Util.*, 2018, **23**, 200–211.
50 N. F. Sulaiman, W. A. Wan Abu Bakar, S. Toemen, N. M. Kamal and R. Nadarajan, *Renewable Energy*, 2019, **135**, 408–416.
51 M. Han, Z. Wang, Y. Xu, R. Wu, S. Jiao, Y. Chen and S. Feng, *Mater. Chem. Phys.*, 2018, **215**, 251–258.
52 N. Habibi, Y. Wang, H. Arandiyan and M. Rezaei, *ChemCatChem*, 2016, **8**, 3600–3610.
53 S. Iglesias-Vázquez, J. Valecillos, A. Remiro, J. Bilbao and A. G. Gayubo, *Catalysts*, 2022, **12**, 550.
54 B. M. Al-Swai, N. B. Osman, A. Ramli, B. Abdullah, A. S. Farooqi, B. V. Ayodele and D. O. Patrick, *Int. J. Hydrogen Energy*, 2021, **46**, 24768–24780.
55 R. Kumari and S. Sengupta, *Int. J. Hydrogen Energy*, 2020, **45**, 22775–22787.
56 Q. Zhang, X. Feng, J. Liu, L. Zhao, X. Song, P. Zhang and L. Gao, *Int. J. Hydrogen Energy*, 2018, **43**, 11056–11068.
57 R. Zhao, K. Cao, R. Ye, Y. Tang, C. Du, F. Liu, Y. Zhao, R. Chen and B. Shan, *Chem. Eng. J.*, 2024, **491**, 151966.
58 F. Schrenk, L. Lindenthal, H. Drexler, G. Urban, R. Rameshan, H. Summerer, T. Berger, T. Ruh, A. K. Opitz and C. Rameshan, *Appl. Catal., B*, 2022, **318**, 121886.
59 E. Pawelczyk, I. Wysocka, T. Dymerski and J. Gębicki, *Catal. Today*, 2024, **427**, 114414.
60 N. D. Charisiou, L. Tzounis, V. Sebastian, S. J. Hinder, M. A. Baker, K. Polychronopoulou and M. A. Goula, *Appl. Surf. Sci.*, 2019, **474**, 42–56.
61 F. Gholizadeh, A. Izadbakhsh, J. Huang and Y. Zi-Feng, *Microporous Mesoporous Mater.*, 2021, **310**, 110616.
62 A. S. Al-Fatesh, Y. Arafat, S. O. Kasim, A. A. Ibrahim, A. E. Abasaeed and A. H. Fakeeha, *Appl. Catal., B*, 2021, **280**, 119445.
63 Z. Alipour, M. Rezaei and F. Meshkani, *J. Ind. Eng. Chem.*, 2014, **20**, 2858–2863.
64 K. Song, M. Lu, S. Xu, C. Chen, Y. Zhan, D. Li, C. Au, L. Jiang and K. Tomishige, *Appl. Catal., B*, 2018, **239**, 324–333.
65 A. N. T. Cao, H. H. Nguyen, T.-P. T. Pham, L. K. H. Pham, D. Ha Le Phuong, N. A. Nguyen, D.-V. N. Vo and P. T. H. Pham, *J. Energy Inst.*, 2023, **108**, 101252.
66 S. Das, M. Sengupta, J. Patel and A. Bordoloi, *Appl. Catal., A*, 2017, **545**, 113–126.
67 B. Jin, S. Li and X. Liang, *Fuel*, 2021, **284**, 119082.
68 P. Cao, H. Zhao, S. Adegbite, B. Yang, E. Lester and T. Wu, *Fuel*, 2021, **298**, 120599.